JOURNAL OF GEOPHYSICAL RESEARCH, VOL. 105, NO. B2, PAGES 2937–2853, FEBRUARY 10, 2000

Precise relocations and stress change calculations for the Upland earthquake sequence in southern California

Luciana Astiz, Peter M. Shearer, and Duncan C. Agnew

Institute of Geophysics and Planetary Physics, Scripps Institution of Oceanography, University of California, San Diego, La Jolla

Abstract. We relocate earthquakes that occurred near the 1988 ($M_L = 4.7$) and the 1990 ($M_L = 5.5$) Upland, California, earthquakes to map the fault geometry of the poorly defined San Jose fault and to test the static stress triggering hypothesis for this sequence. We adopt the L1 norm, waveform cross-correlation method of *Shearer* [1997] to obtain precise relocations for 1573 events between 1981 and 1997 in the Upland area. To limit computation time, we only perform waveform cross correlation on 60 of the nearest neighbors of each relocated event. Our final relocations show two linear features. The first is imaged by the locations of the initial month of aftershocks of the 1988 Upland earthquake, which delineate a fault with a dip angle of ~45° between 7 and 9 km depth, consistent with the mainshock focal mechanism. The second linear feature is a plane dipping at about 74° from 2 to 9 km depth, which is illuminated by both the 1988 and 1990 Upland sequences, in agreement with the inferred location of the San Jose fault at depth. However, below 9 km the event locations become more diffuse, giving rise to two different interpretations of the fate of the San Jose fault at depth. One possibility is that the fault shallows at depth, consistent with our relocations but not with the focal mechanism of a $M_L = 4.7$ deep aftershock. Alternatively, the fault may be offset at depth by the more shallow dipping fault strand broken during the 1988 earthquake. Using these inferred fault geometries, we compute stress changes resulting from slip during the mainshocks to test whether the relocated aftershocks are consistent with the hypothesis that more aftershocks occur where the change in static Coulomb failure stress is positive (on faults optimally oriented for failure). This requires an extension of previous models of changes in the failure stress to three dimensions and arbitrary fault orientation. We find that patterns of change in Coulomb failure stress differ little between the different fault geometries: all are nearly symmetric about the fault and so do not match the aftershock distribution, in which most of the off-fault events occur to one side of the fault plane.

1. Introduction

The tectonics of the Los Angeles region are complicated, characterized by both thrust faulting such as the Whittier Narrows and Northridge earthquakes [e.g., *Hauksson and Jones*, 1989; *Hauksson et al.*, 1995; *Rubin et al.*, 1998; *Shaw and Shearer*, 1999] and strike-slip faulting such as the Pasadena and Upland earthquakes [e.g., *Jones et al.*, 1990; *Hauksson and Jones*, 1991; *Walls et al.*, 1998]. The 1988 and 1990 Upland earthquakes ($M_L = 4.7$ and 5.5, respectively), located in the eastern San Gabriel Mountains in southern California, occurred close to the frontal fault zone of the Transverse Ranges (Figure 1). Studies of background seismicity in the Upland region identify a variety of focal mechanisms [*Cramer and Harrington*, 1987; *Hauksson*, 1990], suggesting a complex tectonic regime in this area. The focal mechanisms of the Upland earthquakes are well constrained from first motion data [*Hauksson and Jones*, 1991] and waveform modeling [*Mori and Hartzell*, 1990; *Dreger and Helmberger*, 1990, 1991], indicating left-lateral, strike-slip motion on the poorly known, northeast trending San Jose fault (Figure 1). Previous studies of the Upland sequences do not entirely explain the relative locations and focal mechanisms of the mainshocks and their aftershocks. In particular, they fail to explain the discrepancy between the 42° dip direction obtained for the 1988 Upland earthquake at ~10 km depth and the 75° dip indicated by aftershock locations down to 13 km depth and by most of the larger aftershock focal mechanisms [*Hauksson and Jones*, 1991, Figures 5 and 6].

Paper number 1999JB900336.
0148-0227/00/1999JB900336$09.00

Direct constraints on the geometry of the San Jose fault are limited. *Woodford et al.* [1944] mapped a steep fault that followed the north side of the San Jose Creek and continued westward into the San Jose Hills. More recently, it has been mapped solely on the basis of a water barrier [*California Department of Water Resources*, 1970], and its surface trace is covered by Holocene sediments. Geodetic data for the central San Gabriel Mountains west of the Cucamonga fault indicate north-south contraction of 5.0 ± 1.0 mm/yr in this area [*Feigl et al.*, 1993] that is being accommodated by conjugate fault slip along the San Jose, Chino, Raymond, and Verdugo faults by east-west extrusion of the Transverse Range Block [*Humphreys*, 1995; *Walls et al.*, 1998].

Aftershock locations are one of the primary tools used by seismologists to constrain fault locations and orientations and are of key importance in unraveling the details of the Upland sequence. However, the accuracy of standard locations is limited by picking errors and three-dimensional velocity variations. Recently, *Shearer* [1997] showed that greatly improved locations could be obtained for southern California earthquakes using the L1 norm and waveform cross correlation. Here we apply this technique to 1573 events in the Upland sequence. Our final relocations show that the first month of 1988 Upland aftershocks delineate a fault with a dip angle of about 45° between 7 and 9 km depth, consistent with the focal mechanism determined from first motion data [*Hauksson and Jones*, 1991], the source-time-function inversion results of *Mori and Hartzell* [1990], and modeling of TERRAscope broadband data by *Dreger and Helmberger* [1990]. This lineation of events seems to offset a steeper fault of ~75° dip, as indicated by the relocations of the first month of 1990 Upland aftershocks, which are consistent with waveform modeling [*Dreger and Helmberger*, 1991] and first-motion data of the 1990 mainshock and its largest aftershocks.

Aftershock locations also are used to test the hypothesis that static stress changes produced by earthquakes increase the probability of events in regions where the Coulomb failure stress (CFS) is increased. Several studies have found correlations between CFS changes and aftershock distributions, suggesting that static stress triggering is significant [e.g., *Reasenberg and Simpson*, 1992; *Stein et al.*, 1992; *Harris and Simpson*, 1992; *King et al.*, 1994; *Stein et al.*, 1994; *Hodgkinson et al.*, 1996; *Harris*, 1998; *Hardebeck et al.*, 1998]. Such studies are most easily carried out for large earthquakes such as the 1992 Landers ($M_W = 7.3$) and 1994 Northridge ($M_W = 6.7$) events where many of the aftershocks are well-separated from the mainshock fault plane and the aftershock regions are much larger than the uncertainties in the locations. It is important, however, to extend these analyses to smaller earthquakes to further test the CFS triggering hypothesis. We use Upland fault geometries inferred from our aftershock locations, together with the slip distribution estimate of *Dreger and Helmberger* [1991], to compute the change in the stress tensor produced by the 1988 and 1990 events. We then calculate the change in the CFS on optimally oriented faults, generalizing the method of *King et al.* [1994] to include three-dimensional fault geometries. Our results show that locations of the Upland aftershocks are not explained by the CFS model. The pattern of stress change is nearly symmetric about the San Jose fault, whereas our precise relocations of the Upland events show that most of the aftershocks that are well off the fault plane lie on the northwest side of the San Jose fault. We speculate, therefore, that factors other than CFS changes, such as asymmetries in the rock properties bounding the fault, are responsible for the observed Upland aftershock distribution.

2. Previous Studies and Archived Data

On June 26, 1988, at 1504 UT, a $M_L = 4.7$ earthquake struck <2 km south of the surface trace of the Cucamonga fault, in a region with little seismicity since 1972 [*Cramer and Harrington*, 1987; *Morton and Matti*, 1987; *Pechmann*, 1987]. This fault defines the easternmost terminus of the Transverse Ranges in southern California. Northeast trending left-lateral, strike-slip faults such as the San Jose and Indian Hill faults are found near its southwest boundary where it joins the Sierra Madre thrust fault (Figure 1). The Southern California Seismic Network (SCSN) catalog location for the 1988 Upland event is at 34.136°N, 117.709°W and 7.9 km depth. Aftershock relocations do not define a clear fault plane and appear inconsistent with the focal mechanism obtained by *Hauksson and Jones* [1991] from 124 first-motion readings for the 1988 mainshock: $\phi = 203°$, $\delta = 42°$, $\lambda = 337°$ (strike, dip, rake). *Mori and Hartzell* [1990] used the empirical Green function approach and determined that the preferred fault plane for this event is the southwest trending plane with the rupture propagating updip, with a slip area of 0.97 km^2, seismic moment of 4.2 $\times 10^{15}$ N m, and a stress drop of 38 bars. They suggested that the 1988 Upland earthquake broke a small left-lateral, southwest trending fault connecting the Cucamonga and Sierra Madre thrust faults. However, *Dreger and Helmberger* [1990] used waveform modeling of three-component broadband recordings at Pasadena to conclude that the source depth for this event is about 6 km and its seismic moment 6.2×10^{15} N m. They also estimate a smaller source area from the earthquake source-time function, and consequently, their stress drop estimate is an order of magnitude higher for this event (410 bars).

Seismic activity in this region continued at an elevated level until February 28, 1990, at 2343 UT, when a $M_L = 5.5$ earthquake occurred at 34.144°N, 117.697°W and 4.5 km depth (SCSN catalog location). Relocated hypocenters for the numerous aftershocks extend from ~2 to 13 km depth. They delineate a plane that agrees with the first-motion focal mechanism of the mainshock, which indicates pure left-lateral, strike-slip motion: $\phi =$

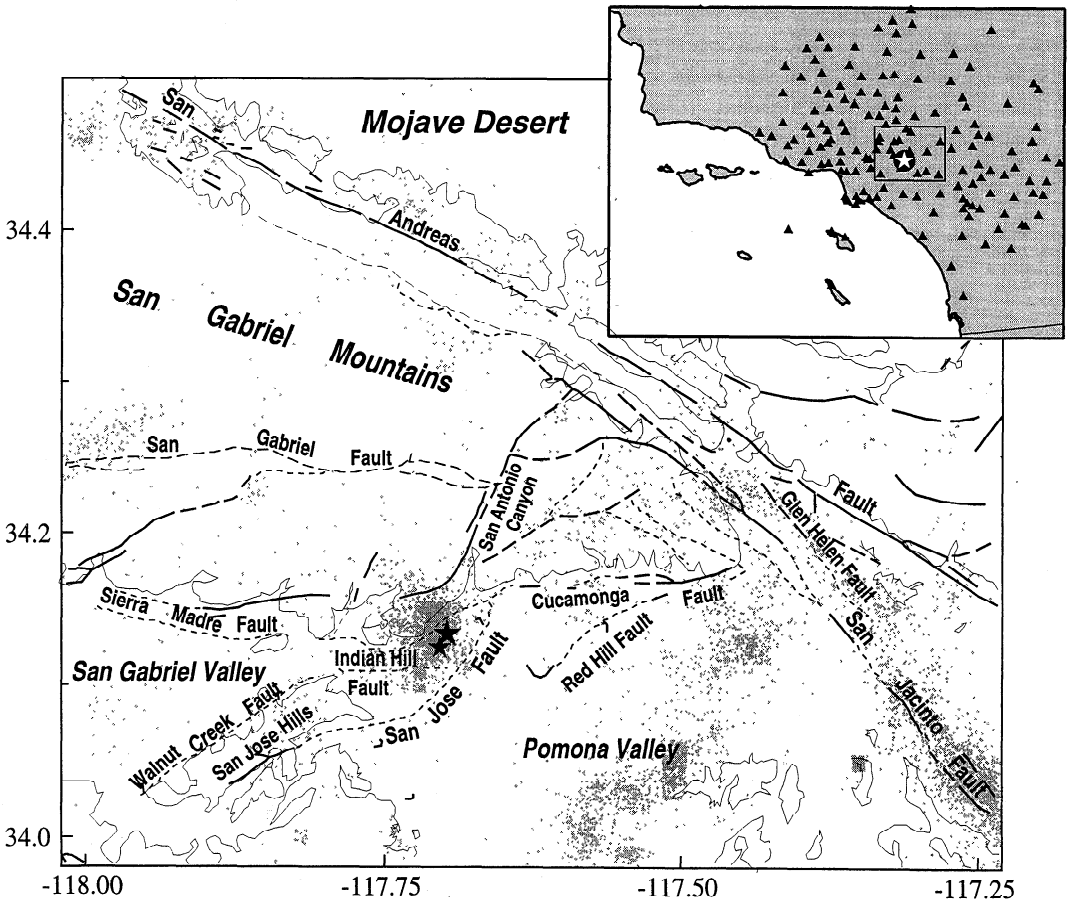

Figure 1. Tectonic map of the eastern San Gabriel Mountains, southern California. Mapped and inferred faults are indicated by thick and dashed lines; thin contours are the contact between basement rocks and alluvial valleys [after *Cramer and Harrington*, 1987]. Light shaded dots are "A" quality earthquake locations from the Southern California Seismic Network (SCSN) catalog. We relocate the cluster of events northwest of the San Jose fault where the 1988 and 1990 Upland earthquakes occurred (indicated by the small and large stars, respectively). The inset map of southern California shows the SCSN stations (triangles) located within 100 km of the Upland area (star).

220°, $\delta = 70°$, and $\lambda = 0°$ [*Hauksson and Jones*, 1991]. *Dreger and Helmberger* [1991] used waveform inversion of three-component broadband Pasadena records to find a similar fault plane solution: $\phi = 216°$, $\delta = 77°$, $\lambda = 5°$, and seismic moment of 2.5×10^{17} N m. They concluded that a complicated source is needed to model the 1990 Upland mainshock waveforms: a rupture initiating at about 6 km depth and propagating downward with most of the moment release occurring near 10 km depth where a bend in the aftershock locations is found [*Hauksson and Jones*, 1991](see Figure 6 below).

The SCSN catalog contains 1573 earthquakes occurring from May 1981 to August 1997 within a box (34.08°N to 34.18°N, 117.75°W to 117.65°W) that encompasses the Upland earthquake sequences. The data set we used contains all events for which picks and waveform data are available through the Southern California Earthquake Center (SCEC) Data Center. We restricted the analysis to the 175 stations that are located within 100 km of the center of this box to ensure that the first arrival is the crustal Pg phase and to avoid uncertainties associated with the Pn crossover distance. The SCSN analysts had picked 21,289 P arrivals and 5155 S arrivals for these events. In general, the number of P and S picks correlates with event magnitude; however, for the largest events, no S picks were reported due to trace clipping at most nearby recording stations. A total of 71,404 waveform traces are available in the archive, many of which had not been picked prior to our analysis.

3. L1 Norm, Grid Search Algorithm, and Station Terms

Computer speeds are now sufficiently fast that grid search methods for earthquake relocation are practical and have the advantage of being readily adaptable to any desired misfit norm [e.g., *Sambridge and Kennett*,

1986; *Kennett*, 1992; *Shearer*, 1997]. The conventional least squares method, or L2 norm (the mean in one-dimensional problems), is optimal when the misfit to the travel times is caused by uncorrelated, random Gaussian noise in the picks. Typically, these assumptions are violated in the Earth and this method may give spurious results due to assigning excessive weight to non-Gaussian outliers in the data. The least absolute value, or L1 norm (the median in one-dimensional problems), weights residuals more equally in the inversion and is considered more robust to data outliers. The effects of these and other misfit norms on the earthquake location problems were explored by *Anderson* [1982] and *Kijko* [1994]. In southern California we have found that L1 norm locations show much less scatter, particularly in depth, than L2 norm locations [*Shearer*, 1997, 1998].

To relocate the Upland sequences, we use a smoothed version of the standard southern California velocity model of *Hadley and Kanamori* [1977][see *Shearer*, 1997, Figure 3]. This model produces smooth travel time curves that can be easily interpolated in range and depth without generating artifacts due to edge effects. A scaled version of the P model is used as a reference S velocity model, assuming a Poisson's ratio of 0.25. From these velocity models we compute P and S travel time tables to a three-dimensional grid that surrounds the events. The location volume is a 20-km cube, resulting in $21^3 = 9261$ grid points separated by 1 km. We determine the distance from each of these grid points to the 175 stations located within 100 km of the center of the cube and obtain predicted P and S travel times from each grid point to each station by interpolating from the travel time tables. Note that this array needs to be calculated only once and can then be used to locate all the events within the volume. For each event the observed P and S wave arrival time picks for all stations are compared to those predicted at each grid point and the best fitting grid point is identified. The location is then further refined by examining a finer grid obtained by interpolating between adjacent grid points. All locations shown in this paper are computed to a nominal resolution of 15 m.

As in the work by *Shearer* [1997], we use a single set of station terms to account for three-dimensional velocity heterogeneity outside of the source region. We compute station terms as the median (L1 norm) of the residuals from all the events to each station. We then relocate the events using these station terms, compute a new set of station terms, and so on (as described by *Frohlich* [1979]). This procedure converges rapidly to a stable solution after only a few iterations. We calculate separate station terms for P and S arrivals using a minimum of five picks to each station. In the final iteration we only use stations with associated station terms. Most station terms are less than ± 0.5 s for the Upland relocations, and they do not have a clear dependence with range that would suggest a problem with the reference one-dimensional velocity model. Locations obtained using these station terms are similar to those previously obtained by *Hauksson and Jones* [1991] using the VELEST code of *Roecker and Ellsworth* [1978].

4. Waveform Cross Correlation With Natural Neighbors

Differential times derived from waveform cross correlation between similar event pairs have proven useful for improving relative earthquake locations in a number of previous studies [e.g., *Poupinet et al.*, 1984; *Ito*, 1985; *Fremont and Malone*, 1987; *Xie et al.*, 1991; *Deichmann and Garcia-Fernandez*, 1992; *Got et al.*, 1994; *Nadeau et al.*, 1995; *Haase et al.*, 1995; *Dodge et al.*, 1995; *Gillard et al.*, 1996]. Since many of the waveforms recorded by the SCSN do not have pick data associated with them, waveform cross correlation of event pairs can be used to obtain additional arrival times as well as improve the consistency of the existing picks. In 1983 the SCSN sample rate increased from 50 to 62.5 Hz, while between 1986 and 1992 it fluctuated between 62.5 and 100 Hz before permanently changing to 100 Hz. For our analyses we resampled the waveforms to a uniform 100-Hz sample rate. Because we found that the waveform cross correlation is more stable at lower frequencies, we also applied a 10-Hz low-pass filter to the traces.

For large numbers of earthquakes it is impractical to compute cross-correlation functions among all event-station combinations. For n events in a sequence, $n(n-1)/2$ event pairs are possible, resulting in over 1.2 million cross correlations per station per phase in the Upland sequence. However, widely separated events are unlikely to yield waveforms that are similar enough that they can be accurately cross-correlated. Waveforms of closely located events have been observed to have higher correlation coefficients than more separated events [e.g., *Pechmann and Kanamori*, 1982; *Pechmann and Thorbjarnardottir*, 1990; *Mezcua and Rueda*, 1994]. Thus, to reduce computation time, we only apply waveform cross correlation to a limited number of nearby events. A key feature of our approach is the way in which we choose these neighboring events.

We select nearby events using the concept of Delaunay tesselation and natural neighbors, methods widely used in computational geometry but only recently introduced to geophysics [e.g., *Parker et al.*, 1987; *Hildebrand and Parker*, 1987; *Constable et al.*, 1993; *Sambridge et al.*, 1995; *Braun and Sambridge*, 1995]. For a given set of points in three dimensions, the Delaunay tesselation specifies connections between the points, or nodes, that define tetrahedra that are as "well-shaped" as possible. The "natural neighbors" of each point are those points that are directly connected by the Delaunay tesselation; they are the closest surrounding points and are uniquely defined by the nodal distribution. Here we generalize this concept, terming those points di-

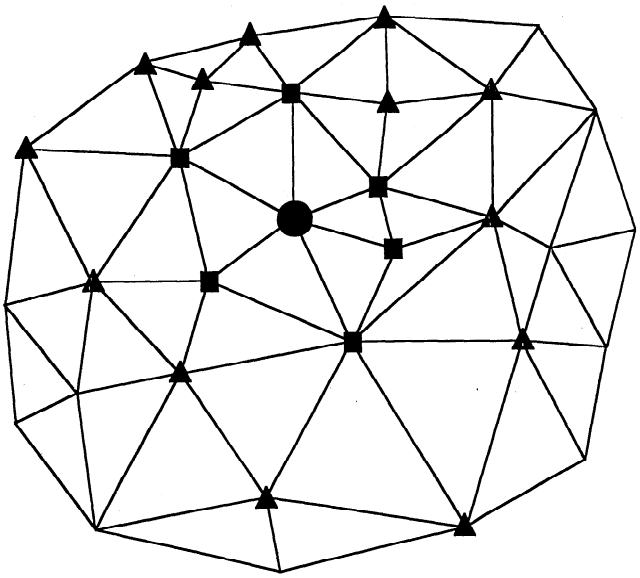

Figure 2. A cartoon illustrating the Delaunay tessellation nearest-neighbor algorithm. The circle represents the target event, squares are the first-order natural neighbors to this event, and triangles are the second-order natural neighbors.

rectly connected by the tesselation as "first-order" natural neighbors, those points connected through a single intervening point as "second-order" natural neighbors, etc.

Using our initial event locations, we compute the Delaunay tessellation and identify a prescribed number of natural neighbors for each event. This is illustrated in two dimensions in Figure 2. The circle represents the target event, the squares are the first-order natural neighbors to this event, and the triangles are the second-order natural neighbors to the target event. The number of first- and second-order natural neighbors is not fixed but will vary from event to event depending upon the geometry of the tesselation. Our strategy is to chose m nearest neighbors by first randomly selecting from the pool of first-order natural neighbors and then, if this does not provide enough events, by randomly selecting from the second-order neighbors. For $m = 60$, we did not have to go beyond the second-order natural neighbors for the Upland events. Depending upon the density of the events surrounding the target event, the nearest neighbors can span a wide range of distances (i.e., <20 m to >1 km). The Delaunay tesselation en-

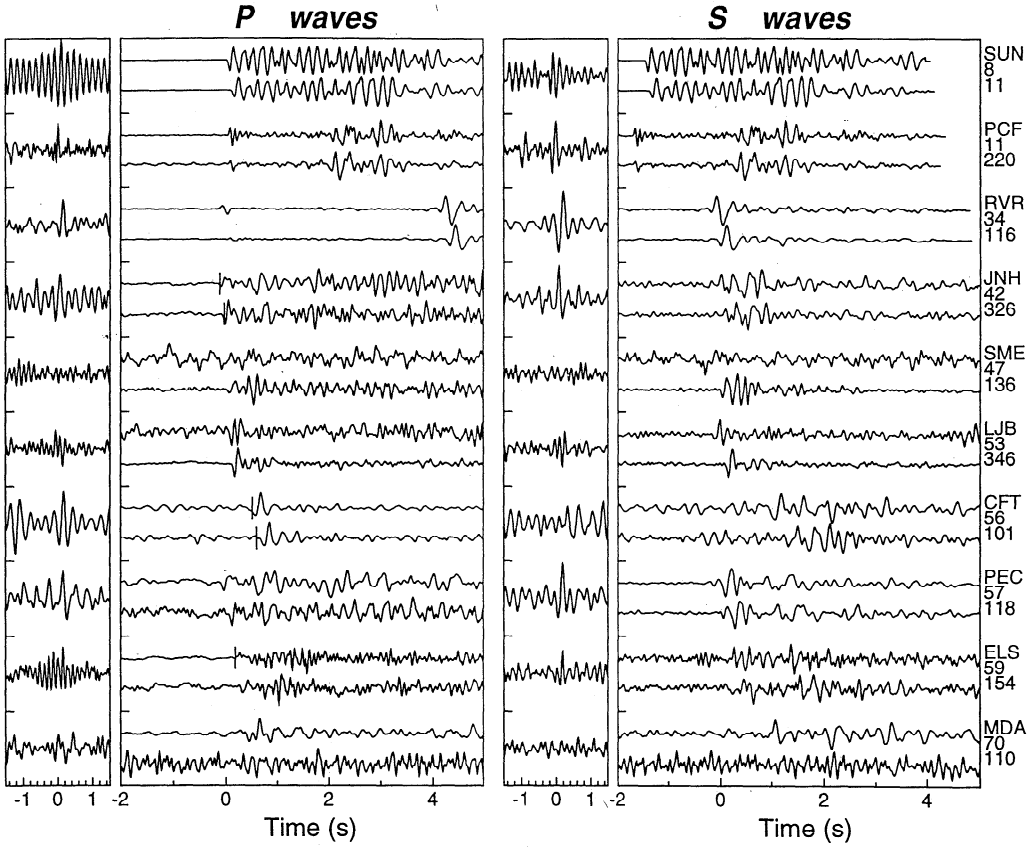

Figure 3. Waveform cross correlation applied to a pair of similar earthquakes from the Upland sequences, a $M_L = 2.1$ event (June 26, 1988, 1846 UT) and a $M_L = 1.8$ event (March 4, 1990, 0220 UT). The larger panels show the P and S waves recorded at the 10 stations listed to the right; the source-receiver distance in kilometers and azimuth to each station are also indicated. The traces have been low-pass filtered at 10 Hz. SCSN analyst picks are indicated by tic marks. The smaller panels show the cross-correlation functions computed using 2- and 3-s windows around the P and S waves, respectively. Note that about half of the pairs show a well-defined maximum that can be used as a measure of the differential time between the traces.

Table 1. Number of P and S Picks

	Median Picks per Event		Total Number of Picks	
	P Picks	S Picks	P Picks	S Picks
SCSN picks	11	3	21,289	5,155
Adjusted picks (m=30)	15	9	27,245	14,052
Adjusted picks (m=60)	15	10	27,253	14,771

sures that the subset of event pairs that we choose are linked in such a way that every event is "connected" to even the most distant events by a chain of event pairs. This approach reduces the number of required event cross correlations to order $nm/2$. Note that for fixed m the computational cost grows linearly with n, rather than as n^2, so that large problems become more tractable. For the Upland sequence we experimented with both $m = 30$ and $m = 60$ in the selection of the event pairs and found that the $m = 60$ produced somewhat better results (see below).

The cross-correlation procedure is illustrated in Figure 3 by a pair of similar earthquakes from the Upland sequences, a $M_L = 2.1$ event (June 26, 1988, 1846 UT) and a $M_L = 1.8$ event (March 4, 1990, 0220 UT). Note that about half of the pairs show a well-defined maximum that can be used as a measure of the differential time between the traces. Event clusters that are connected by at least one differential time path for a given threshold correlation coefficient are termed "trees" [*Aster and Scott*, 1993]. We require a minimum cross-correlation coefficient of 0.45 for at least 10 event pairs for a given station to form a tree from which differential times between stations are determined.

Following waveform cross correlation, we solve for a new set of arrival times that best fit both the differential times (provided by the waveform cross correlation) and the original picks. This procedure provides what we term "adjusted" P and S picks and is described in detail by *Shearer* [1997]. Originally, the SCSN analysts had picked 21,289 P and 5155 S arrival times. After cross correlation of the Upland events with their nearest neighbors to obtain differential times and inversion of the observed and differential times between events, we added about 6000 new P picks and almost tripled the total number of S picks available for the events (see Table 1). We increased the median number of P arrival times for each event from 11 to 15 and from 3 to almost 10 for the S picks. The increased number of arrival times contributes to better event locations; in particular, the addition of S picks is critical for obtaining more accurate event depths (as noted by *Gomberg et al.* [1990]). The histograms in Figure 4 show the number of P (Figure 4, top) and S (Figure 4, bottom) arrival times; light shaded bars are the original SCSN analyst picks, and dark shaded bars are the adjusted picks after waveform cross correlation (with 60 natural neighbors) is applied for each event in the sequence. Although the increase in the number of P arrival times is moderate (see Figure 4, top), the increase in the number of S picks is noteworthy. Before cross correlation, only about 200 events had more than five S picks, but after cross correlation, over 1000 of the events have more than five S picks, with over 500 having more than 10 S picks (see Figure 4, bottom). We observe that increasing the number of target events increases the number of additional picks but mainly for larger-magnitude events.

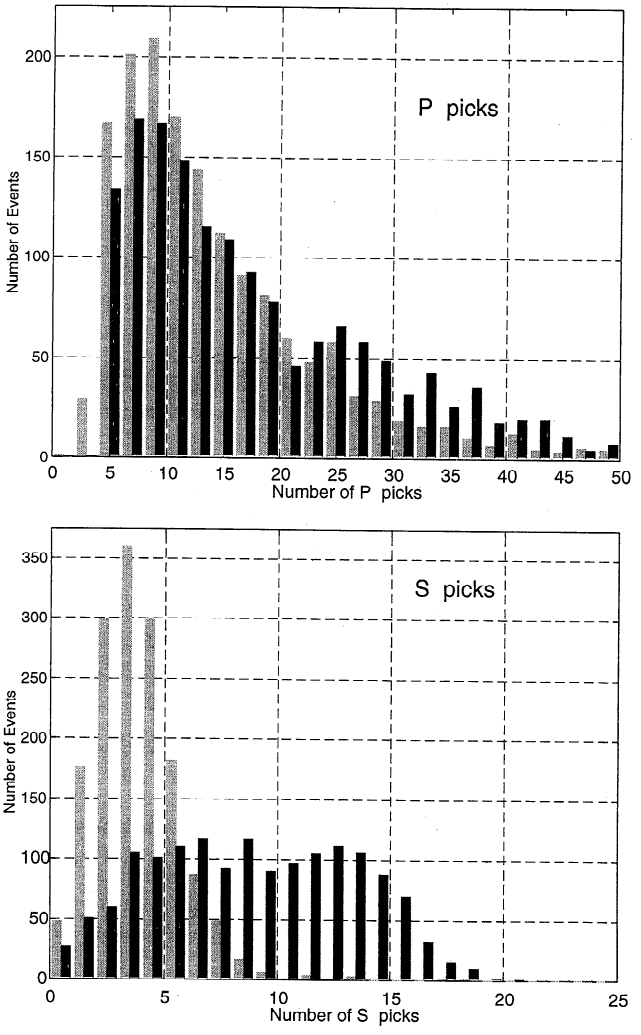

Figure 4. Comparison of number of (top) P and (bottom) S picks from the original SCSN catalog (light bars) and the adjusted arrival times obtained after cross correlation with the 60 nearest neighbors to each event (dark bars). The number of P picks increases from the original 21,289 to 27,253 after cross correlation, i.e., about three more P picks per event. The S picks increase almost threefold from the original 5155 in the SCSN catalog to 14,771, yielding about five more S picks per event for the Upland sequence.

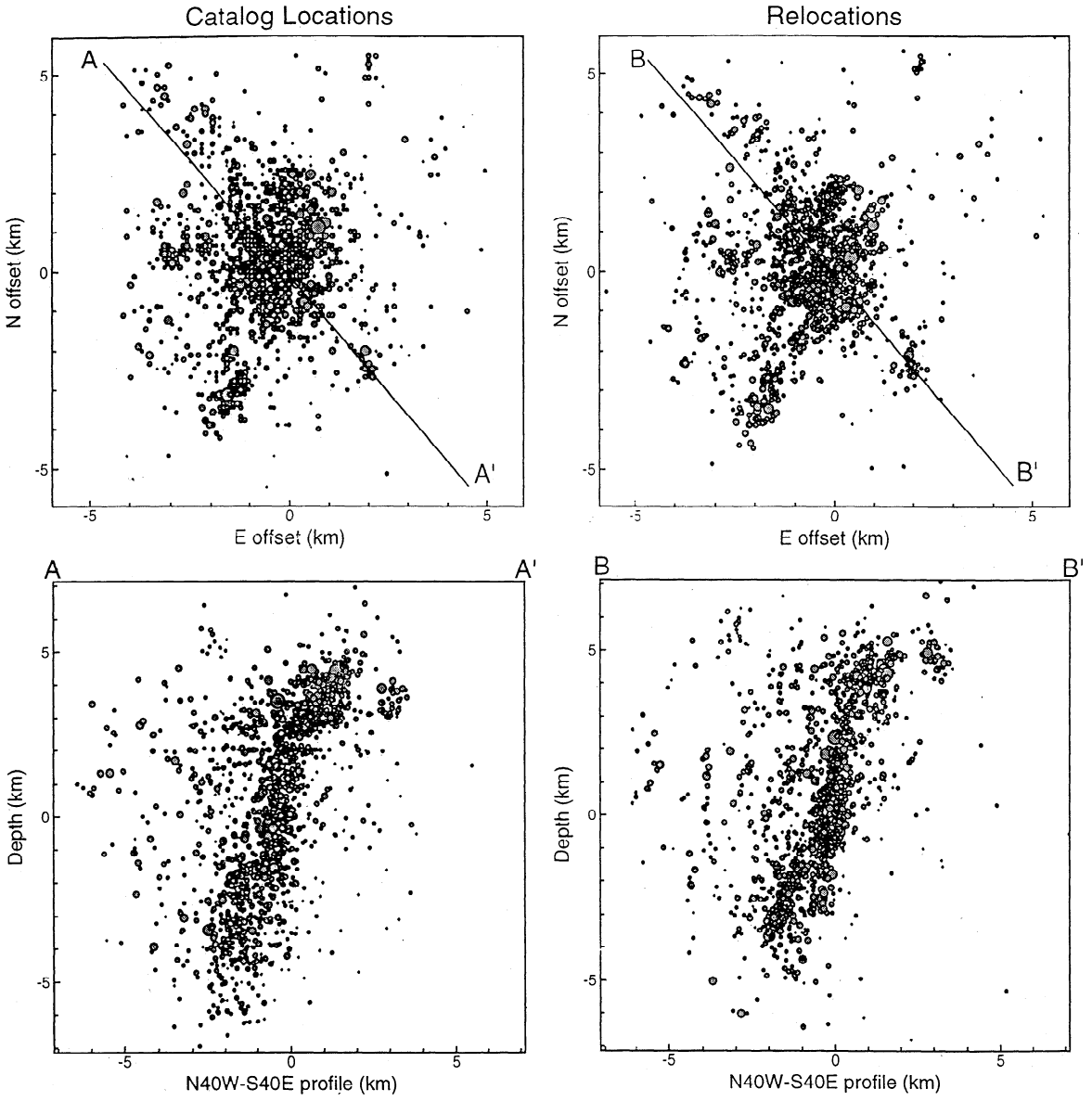

Figure 5. A comparison between (left) southern California catalog locations for the Upland events and (right) our final relocations using the adjusted picks. (top) Map views assuming a reference location of 34.134°N and 117.704°W. (bottom) Along-strike vertical cross sections along N40°W - S40 °E.

Using the adjusted picks, we relocate the events in the Upland sequence using the L1 norm grid search algorithm described above (this includes computation of a new set of station terms). The results show some improvement (as measured by the scatter in the locations) compared to the locations obtained prior to waveform cross correlation. Figure 5 shows a comparison of the original southern California catalog locations and our final relocations using the adjusted picks for 1510 of the Upland events classified as quality A locations in the SCSN catalog (i.e., horizontal errors <0.5 km and vertical errors <1.0 km). The improvement in the locations is apparent but not as dramatic as that obtained for the Whittier Narrows aftershocks by *Shearer* [1997]. This is probably due to the fact that the errors in the catalog locations are greatest in depth, thus not showing up as clearly for a steeply dipping fault such as Upland compared to the shallow dip of the Whittier Narrows aftershocks. Nonetheless, our relocations show greater clustering and more detail than the catalog locations, and the one-sided nature of the off-fault aftershocks is more clearly defined.

5. Estimating Location Uncertainties

We estimate location errors using the random resampling method described by *Billings et al.* [1994] and *Shearer* [1997]. The travel time residuals resulting from each event location are assumed to represent random timing errors. We simulate the effect of these errors

Table 2. Median Standard Errors in Locations

	Original Picks	Adjusted Picks	
		m=30	m=60
Horizontal error, km	0.117	0.089	0.089
Vertical error, km	0.272	0.221	0.205

on the computed location by randomly selecting residuals (from the complete set of residuals for the event) to add to each arrival time, and then we relocate the event using these perturbed arrival times. By repeating this procedure many times, we obtain a cloud of possible locations for the event that represents the scatter due to uncertainties in the picks. This technique has the advantages of fully including all of the nonlinearities in the problem and the fact that some stations and ray paths are much more important than others in constraining the location. Note that these error estimates are a measure of relative location errors among the events produced by random errors in the arrival times. They do not include the systematic errors introduced by incorrect velocity models or three-dimensional velocity heterogeneity. These factors introduce additional uncertainty into the absolute location for all of the events [e.g., *Pavlis*, 1986, 1992]. In particular, our use of a single set of station terms for all of the Upland events does not fully account for the effects of three-dimensional velocity structure. The effects of this structure may be absorbed into the locations so that the final residuals are small even though the locations are significantly biased.

Median standard error estimates for each location procedure are summarized in Table 2. The horizontal errors (h_{err}) of the relocations that included additional picks improved with respect to those determined only with the original picks, but the $m = 60$ (number of nearest neighbors selected for waveform cross correlation) estimated errors were no better than the $m = 30$ errors. However, the median estimated vertical errors (z_{err}) are smaller for $m = 60$ compared to $m = 30$. The images obtained from the adjusted picks resulting from cross correlation of the events using $m = 60$ are noticeably clearer than those obtained using $m = 30$, and the number of events with smaller error bounds increased. The horizontal and vertical median standard errors for our best relocations are 90 and 200 m, respectively.

Another way to appraise our final results is provided by a histogram of the travel time residuals (Figure 6). These are sharply peaked at zero as is typical of residuals from L1 norm inversions. A robust measure of the spread in the residuals is given by the scaled median absolute deviation (SMAD), the median absolute value scaled so that SMAD is equal to the standard deviation for a Gaussian distribution. SMAD = 0.030 s for the P wave residuals, and SMAD = 0.044 s for the S wave residuals. This spread appears reasonable, given that the adjusted picks are composed of a mixture of the original SCSN absolute arrival time picks and reassigned picks based on waveform cross correlation among different events.

6. Relocation Results

We relocated 1534 of the original 1573 events. The reduction in number arose from the requirement that each event have at least five arrival time picks and because waveform data were not available for some of the events in the catalog. Figure 7a shows our final relocations, which use the adjusted picks obtained after waveform cross correlation with 60 nearest neighbors for each event. The top panel shows a map view in which the reference location is 34.134°N and 117.704°W. In this and subsequent figures, we plot only those 1385 events (~90% of the original number) with estimated location standard errors $h_{\mathrm{err}} < 0.5$ km and $z_{\mathrm{err}} < 1$ km. Focal

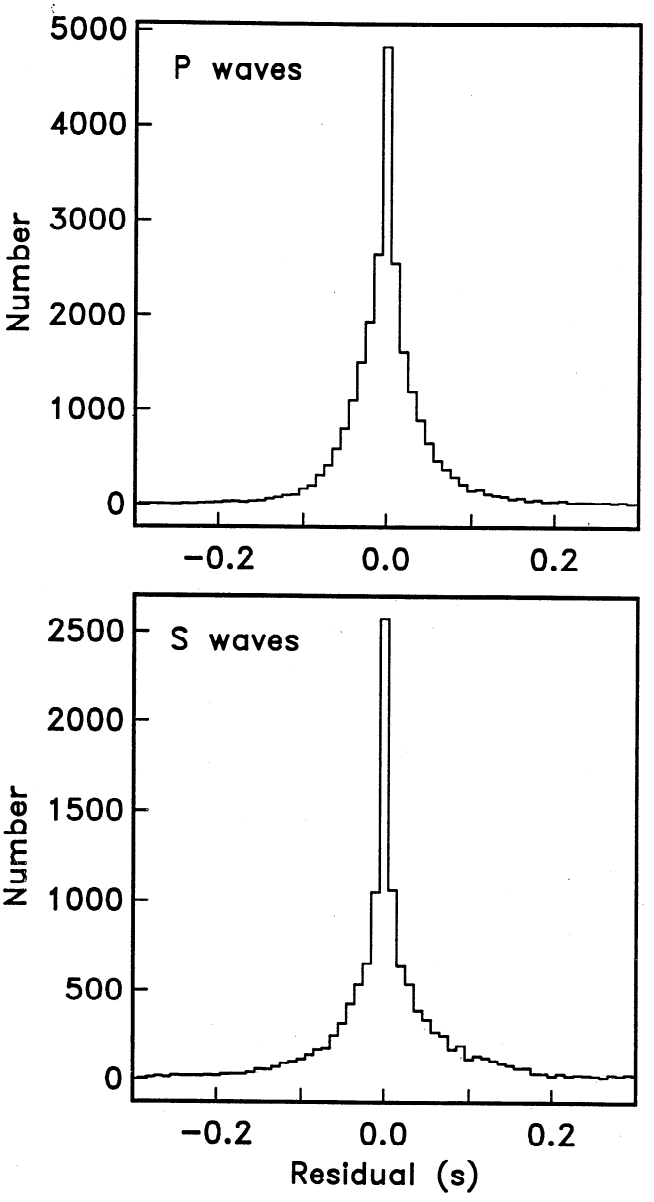

Figure 6. Residual histograms from our final Upland locations for (top) P waves and (bottom) S waves.

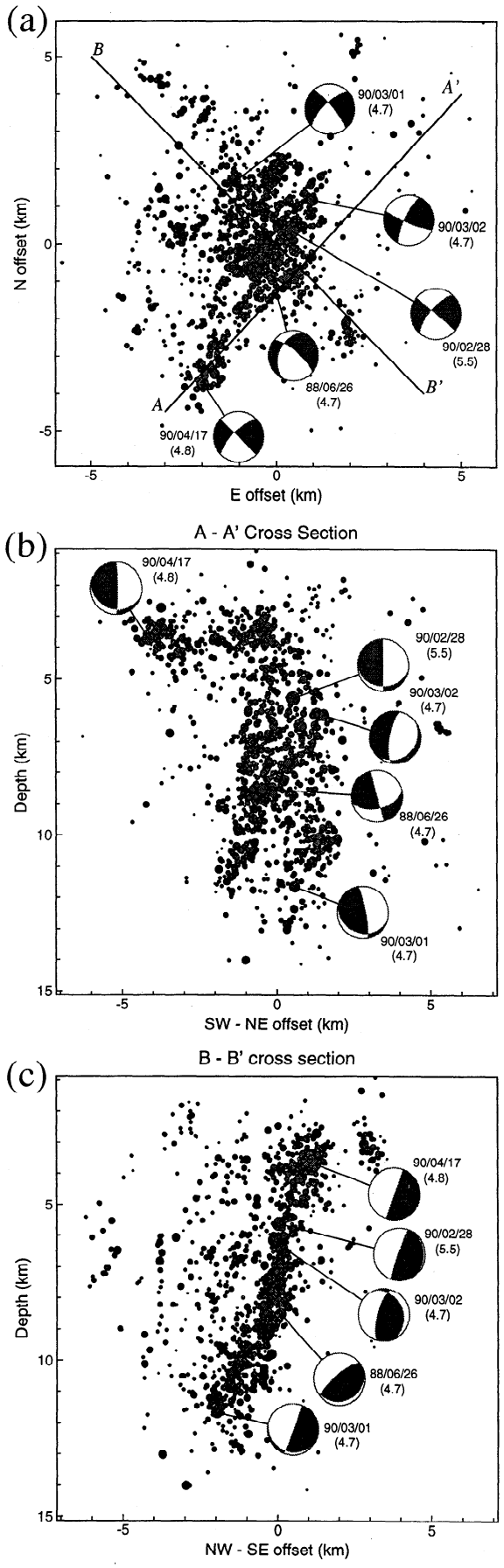

mechanisms for events with $M_L > 4$ are also plotted; the fault plane solutions are from *Hauksson and Jones* [1991] and indicate left-lateral strike slip motion on the San Jose fault [*Cramer and Harrington*, 1987, Figure 1]. Figure 7b is a cross section along the inferred strike of this fault, line A-A′ in Figure 7a. The projection of the relocated events onto the San Jose fault plane shows that most events occurred within a 4-km band between 2 and 13 km depth. Note that very few events occurred below 5 km downdip of the April 17, 1990, mainshock and its aftershocks. The profile in Figure 7c is a vertical cross section along line B-B′ in the top panel, oriented N45°W. Along this profile most events are tightly clustered in a band 1 to 2 km wide. Although the relocated events cluster into a narrow fault plane that seems to shallow at depth (as suggested by *Hauksson and Jones* [1991]), most of the scattered seismicity is relocated to the northwest of the fault plane.

7. Time Evolution of the Upland Sequence

To examine the time dependence of the 1988 ($M_L = 4.7$) and 1990 ($M_L = 5.5$) Upland earthquake sequences, we plot our locations in the time slices indicated in Figures 8 and 9. Figures 8 (left) and 9 (left) are map views, Figures 8 (middle) and 9 (middle) show N45°E vertical cross sections (A-A′, roughly parallel to the strike of the San Jose fault), and Figures 8 (right) and 9 (right) show N45°W cross sections (B-B′). Lower hemisphere focal mechanisms are from *Hauksson and Jones* [1991] for all events with $M > 3.6$ (to include the largest aftershocks of both sequences) and are rotated into each projection plane.

Figure 8 (first row) indicates the pre-1988 Upland seismic activity. There are few events, mostly occurring at shallow depths, and the seismicity does not define any particular fault plane in the B-B′ cross section. Figure 8 (second row) shows seismicity within the first month after the February 26, 1988 Upland earthquake and defines the +1-month aftershock area of 2.6 km^2, which is about a factor of 2 larger than that estimated

Figure 7. (a) A map view of the final relocations using the adjusted picks, assuming a reference location of 34.134°N and 117.704°W. (b) The along-strike vertical cross section A-A′ for the San Jose fault. (c) The B-B′ vertical cross section. Only 1385 events are shown, those with horizontal (h_{err}) and vertical (z_{err}) standard errors <0.5 and 1 km, respectively (~90% of all relocated events). Focal mechanisms for events with $M_L > 4$ [from *Hauksson and Jones*, 1991] are lower hemisphere projections in Figure 7a, and their corresponding projections onto the cross sections are shown in Figures 7b and 7c.

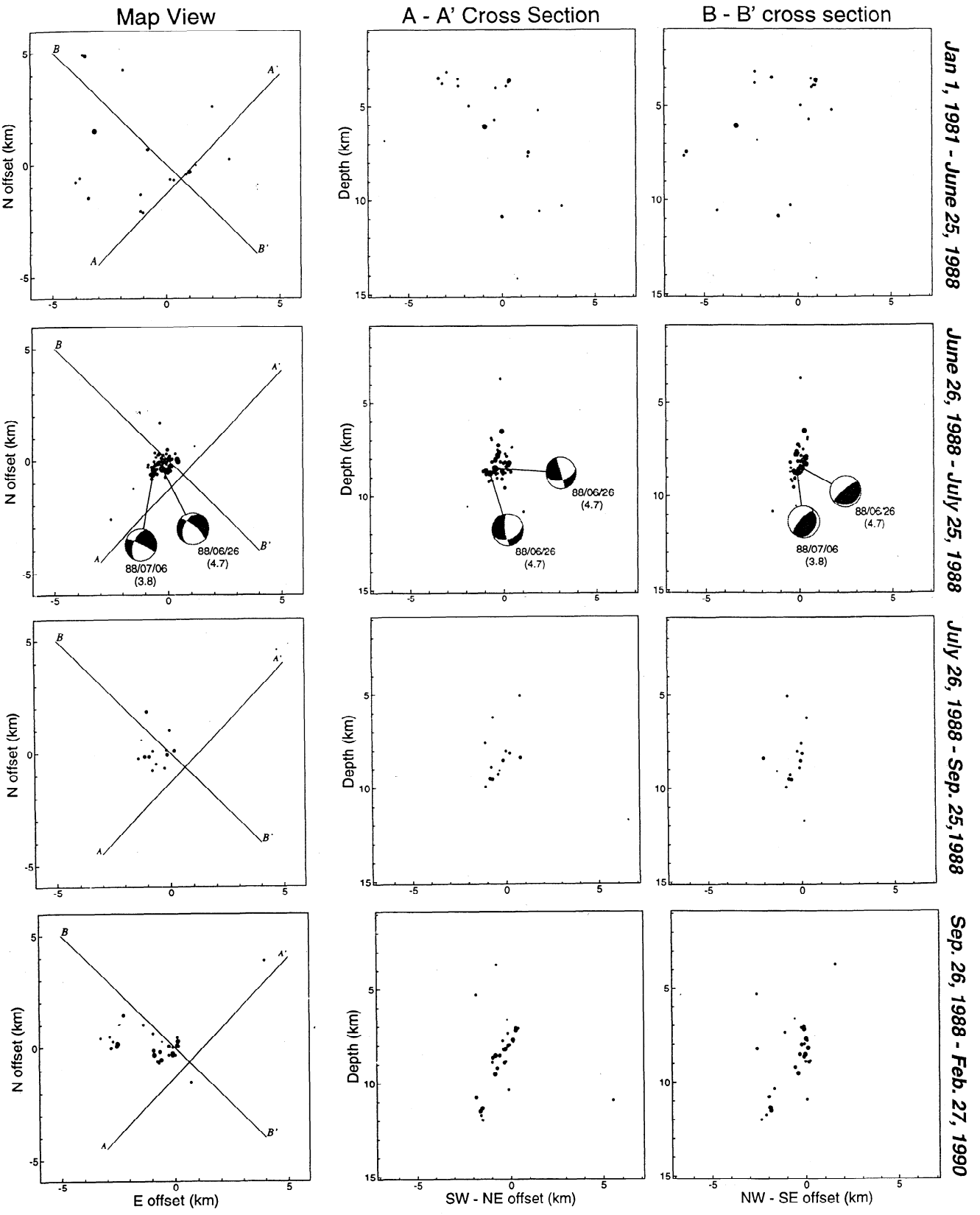

Figure 8. Time slices for the 1988 Upland earthquake ($M_L = 4.7$). (left) Map views, (center) the San Jose fault along-strike A-A′ cross sections, and (right) the B-B′ vertical cross section. Time slices are from top to bottom: pre-1988 Upland earthquake activity, 0 to +1 month activity, +1 to +3 month activity, and the +4 to +17 month activity (up to the time of the 1990 mainshock). The deepest events occurred within 6 months of the 1988 earthquake. Lower hemisphere focal mechanisms of $M_L > 3.6$ events [*Hauksson and Jones*, 1991] are shown in map view and their projections onto the cross sections are shown in the other panels. Only events with $h_{\mathrm{err}} < 0.5$ km and $z_{\mathrm{err}} < 1$ km are shown.

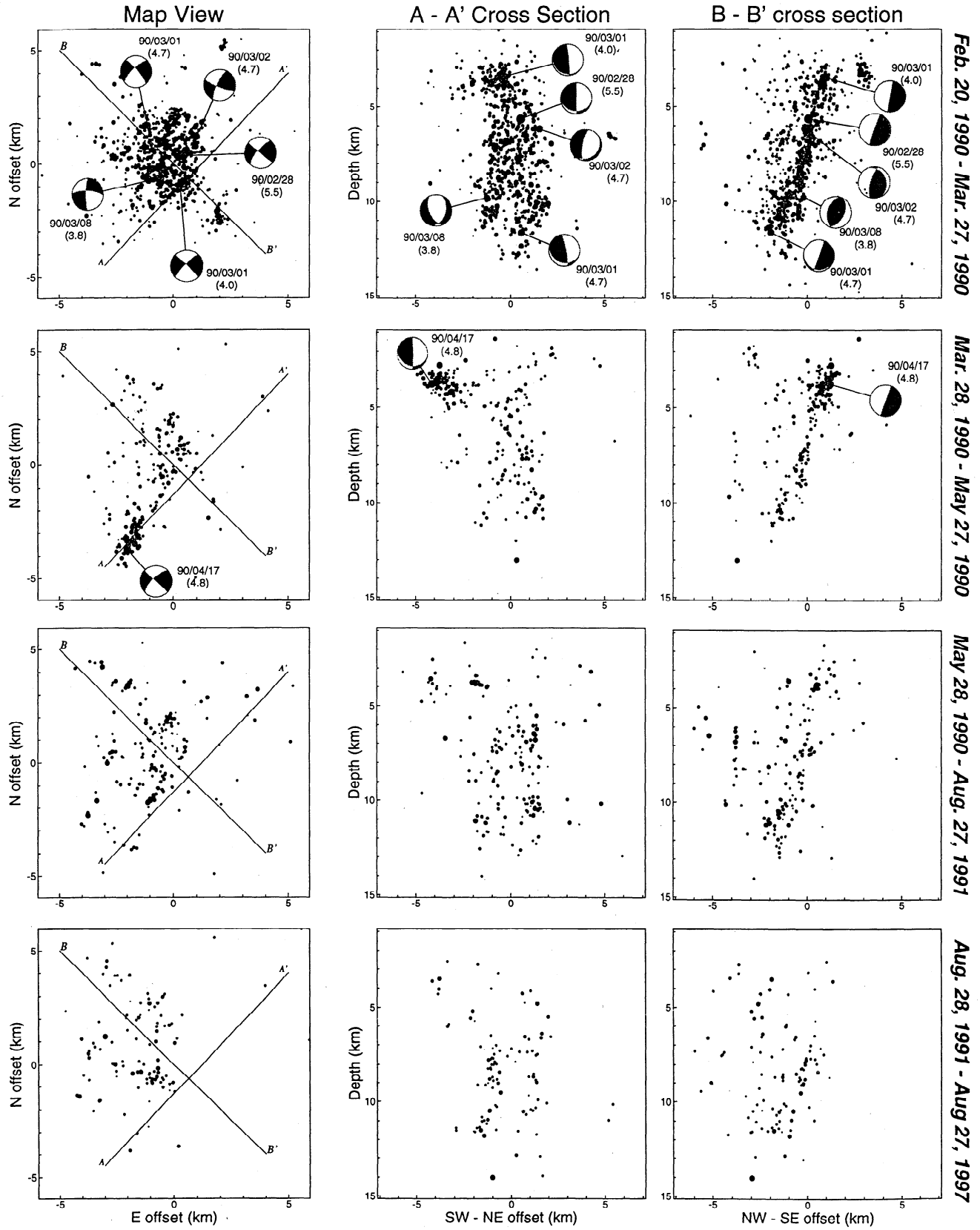

Figure 9. Time slices for the 1990 Upland earthquake ($M_L = 5.5$). (left) Map views, (middle) the San Jose fault along strike A-A′ cross sections, and (right) the B-B′ vertical cross section. Time slices are from top to bottom: 0 to +1 month aftershocks, +1 to +3 month activity, +3 to +18 month activity, and 6 years of post +18 month activity. Lower hemisphere focal mechanism solutions of $M_L > 3.6$ events [*Hauksson and Jones*, 1991] are shown in map view and their projections onto the cross sections are shown in the other panels. Only events with $h_{\text{err}} < 0.5$ km and $z_{\text{err}} < 1$ km are shown.

by *Mori and Hartzell* [1990]. Note that most of these 55 events are located between 8 and 9 km depth and define a plane dipping at about 45° (B-B′ cross section). The dip of the focal mechanisms of the mainshock and its largest aftershock match this seismicity lineation and indicate left-lateral, strike-slip motion along the strike of the San Jose fault in the map view (Figure 1). However, the shallower events seem to delineate a steeper dipping plane, more in agreement with the inferred dip of the San Jose fault [*California Department of Water Resources*, 1970]. Figure 8 (third row) shows 14 events occurring between 1 to 3 months after the 1988 Upland ($M_L = 4.7$) earthquake. Note that the seismicity deepens to about 10 km and delineates a steeper dipping plane. Also note that the deepest event (near 12 km depth) is located outside the main cluster of activity, both in Figure 8 (left) and Figure 8 (middle). In Figure 8 (bottom row) we show the events from the next 17 months up to the time of the 1990 Upland ($M_L = 5.5$) earthquake with the deepest events occurring within 6 months of the 1988 earthquake. Note that the events located between 7 and 10 km depth delineate a steeply dipping plane in the B-B′ cross section and include the $M_L = 2.8$ foreshock that occurred about 3 hours before the 1990 mainshock. Three foreshocks occurred the same day as the 1990 Upland event; all of them were located at least 2 km deeper than the mainshock, near the inferred complexity of the San Jose fault [*Hauksson and Jones*, 1991; *Dodge et al.*, 1996].

Figure 9 shows time slices for the events occurring after the 1990 Upland ($M_L = 5.5$) earthquake. Figure 9 (top row) shows 759 of our relocations that define the +1-month aftershock area of about 32 km^2 (Table 3). The focal mechanism solutions in map view show left-lateral, strike-slip motion on a steep plane, consistent with motion on the San Jose fault as originally proposed by *Hauksson and Jones* [1991]. A cluster of shallow events is located southeast of the trace of the fault. The projection of the hypocenters along the fault strike (A-A′ cross section) outlines a band of activity that broadens with depth. Seen edge on (B-B′ cross section), this seismicity defines a narrow plane of seismic activity from about 2 to 9 km depth. Below this depth the seismicity becomes more diffuse. This increased scatter is unlikely to be a result of location uncertainties in the deeper events because estimated errors in the relocations are uncorrelated with event depth.

Figure 9 (second row) shows the +1 to +3 month seismic activity and include 243 relocated events. These mainly illuminate the broken section of the San Jose fault but also suggest new activity along its shallow southwest section, beginning with a $M_L = 4.8$ earthquake that was followed by numerous aftershocks. Figure 9 (third row) shows 164 of our best relocations that occurred from 3 to 18 months after the 1990 event. They are distributed over the same areas of the fault plane that was active in the preceding 3 months. Although they continue to delineate a steep fault to about 9 km depth, there are more events occurring off this plane, mostly to the northwest. Figure 9 (bottom row) shows the events that occurred between August 28, 1991, and August 27, 1997. During this 6-year period the aftershock activity has continued in a number of areas but at a greatly reduced rate compared to the time intervals more immediately following the mainshocks.

8. Interpretation

We consider three different fault models that explain different features of the seismicity and focal mechanism solutions. All three models have two identical linear features above 9 km but differ below this depth, as illustrated in Figure 10. The first linear feature is a plane dipping at ~74° between ~2 to 9 km depth that is illuminated by both the 1988 and 1990 Upland sequences (see Figures 8 and 9), which agrees with the previously inferred location of the San Jose fault at depth [*California Department of Water Resources*, 1970]. The second feature common to all three models is the small plane imaged from the +1-month aftershock relocations of the 1988 Upland ($M_L = 4.7$) earthquake (Figure 8) that dips at ~45° between 7 and 9 km depth. The strike, dip, and rake of this plane projected on the B-B′ cross-section plane are given in Table 3 (Upl88).

In Figure 10 we plot only the very best 1178 event relocations, with $h_{\mathrm{err}} < 250$ m and $z_{\mathrm{err}} < 500$ m, and compare these to the hypothesized fault geometries of the three models. All models include the plane imaged from the 1988 Upland sequence but have different orientations for the plane that can be imaged from the +1-month aftershocks of the 1990 Upland ($M_L = 5.5$) earthquake (Figure 9). Model 1 has a single steeply dipping fault (Figure 10, top) that only provides a rough fit to the deeper seismicity. Model 2 has a steeply dipping fault that shallows at depth as originally suggested by *Hauksson and Jones* [1991] and hinted by our relocations (Figure 10, bottom left). Model 3 includes a steeply dipping fault with an offset around 9 km depth, consistent with our relocations and the focal mechanism solution of the $M_L = 4.7$ earthquake that occurred at 12 km depth 3 hours after 1990 mainshock. The latter two models are in agreement with the *Dreger and Helmberger* [1991] interpretation of the rupture characteristics of the 1990 Upland earthquake, in which the rupture started at about 6 km and propagated to 9 km depth, where most of the moment release occurred. The shallowing at depth of the San Jose fault depicted on model 2 implies that the San Jose fault joins an unknown shallower dipping fault at depth, whereas model 3 only implies that the tectonic history of this area is complex and that the San Jose fault continues at depth with a similar dip as suggested by the focal mechanisms of the larger aftershocks in the sequence. Model 3 is our prefered model since it is consistent with the aftershock

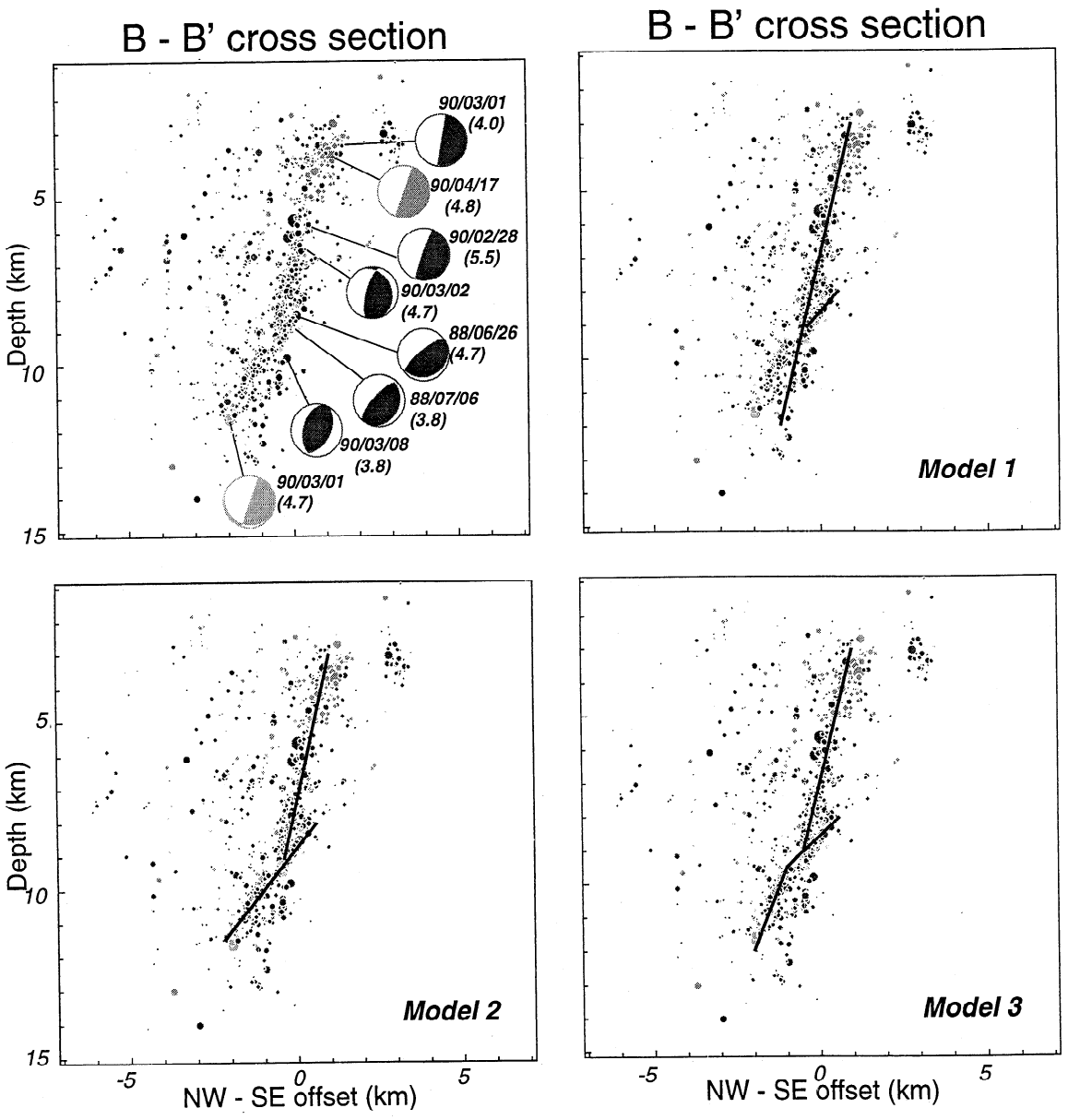

Figure 10. Models for three different possible fault geometries of the Upland sequence overlaid onto the hypocenter locations with $h_{\mathrm{err}} < 250$ m and $z_{\mathrm{err}} < 500$ m. The vertical cross section B-B′ is plotted (see Figure 7); this section is perpendicular to the hypothesized faults (shown as heavy lines). Focal mechanisms from *Hauksson and Jones* [1991] are plotted in vertical cross section (top left).

locations and the focal mechanisms of the larger events and with more recent tectonic models of the area [*Walls et al.*, 1998].

9. Static Stress Change Calculations

One obvious feature of the aftershock distribution in Figures 5 and 7 (especially after relocation) is its asymmetry, with many more events northwest of the main rupture than southeast of it. Several studies have suggested that the aftershock pattern for many earthquakes is related to static stress changes from the mainshock [e.g., *Reasenberg and Simpson*, 1992; *Stein et al.*, 1992; *Harris and Simpson*, 1992; *King et al.*, 1994; *Stein et al.*, 1994; *Hodgkinson et al.*, 1996; *Harris*, 1998; *Hardebeck et al.*, 1998]. In particular, the rate of aftershocks is thought be greater in regions where the Coulomb failure stress (CFS) is increased by the mainshock. Given the high quality of the seismicity distribution determined by our relocation methods, and the availability of a (relatively) detailed rupture model from *Dreger and Helmberger* [1991], the Upland sequence provides a good test of this hypothesis for an event much smaller than any previously studied.

To compare seismicity and stress change without knowledge of the fault planes of the aftershocks, we con-

Table 3. Fault Parameters Used in the Stress Calculations

	Model	Plane	Strike	Dip	Rake	Area, km^2	M_0, N m	
Upl88	all	1	225°	44.44°	-30.95°	2.596	4.2×10^{15}	*
Upl90	1	1	225	71.28	6.69	22.38	2.4×10^{17}	†
Upl90	2	1	225	74.27	6.80	22.38	2.4×10^{17}	†
Upl90	2	2	225	56.76	5.91	10.25	1.5×10^{16}	‡
Upl90	3	1	225	74.39	6.81	22.71	2.4×10^{17}	†
Upl90	3	2	225	71.42	-11.20	9.49	1.5×10^{16}	‡

* Moment from *Mori and Hartzell* [1990].

† Moment from *Dreger and Helmberger* [1991].

‡ This paper using the *Kanamori and Anderson* [1975] magnitude–moment scaling relationship.

vert the tensor stress change caused by the mainshocks into a scalar, the change in Coulomb failure stress, which we term ΔCFS. We follow the procedure of *King et al.* [1994], but that treatment is two-dimensional and assumes strike-slip faulting only. While *Stein et al.* [1994] and *Hodgkinson et al.* [1996] have modifed the treatment to cover other fault types (thrust or normal), we generalize it to an arbitrary fault orientation. Let the ambient stress before the earthquakes be given by the tensor $\mathbf{T}^A$ and the coseismic stress change by the tensor $\mathbf{T}^C$. We compute $\mathbf{T}^C$ from the equations for a dislocation in an elastic half-space, using the DIS3D program of *Erickson* [1986]. The total stress after the earthquakes is then the tensor $\mathbf{T}^T = \mathbf{T}^A + \mathbf{T}^C$, for which we can find the principal axes of stress $\hat{\mathbf{n}}_1$, $\hat{\mathbf{n}}_2$, and $\hat{\mathbf{n}}_3$, corresponding to the largest, intermediate, and smallest principal stresses. (We take compressive stress to be negative, so the largest stress is the most tensional.)

Given a possible failure plane with orientation defined by its normal $\hat{\mathbf{n}}$, and a stress tensor $\mathbf{T}$, the Coulomb failure stress on the plane (the maximum stress to promote slip) is given by

$$\tau + \mu_{fr}(\sigma + p), \tag{1}$$

where $\sigma = \hat{\mathbf{n}} \cdot (\hat{\mathbf{n}} \cdot \mathbf{T})$ is the normal stress, $\tau = |\hat{\mathbf{n}} \cdot \mathbf{T} - \hat{\mathbf{n}}\sigma|$ is the magnitude of the shear stress, μ_{fr} is the coefficient of friction, and p is the pore pressure. We first seek the plane on which this Coulomb stress is maximized for $\mathbf{T}^T$; the Mohr's circle construction for stress in three dimensions shows that this depends only on the largest and smallest principal stresses and has the normal

$$\hat{\mathbf{n}} = \hat{\mathbf{n}}_1 \cos\theta + \hat{\mathbf{n}}_3 \sin\theta, \tag{2}$$

where $\theta = \pi/4 - \text{atan}(\mu_{fr})/2$. Given this direction, the change in Coulomb failure stress, ΔCFS, is given by (1), evaluated for the change in stress $\mathbf{T}^C$. For the Upland calculations, we take μ_{fr} to be 0.4 and ignore any effect of pore fluid pressure.

We compute $\mathbf{T}^C$ for slip models based on the fault geometry models discussed above and the published sizes of the three largest events. First, we include the 1988 ($M_L = 4.7$) mainshock, with the fault plane imaged from our relocations and assuming uniform slip and the *Kanamori and Anderson* [1975] magnitude-moment scaling relationship (this fault has the same geometry in all three of the hypothesized models shown in Figure 10). Second, we include the 1990 ($M_L = 5.5$) mainshock with the slip distributed according to the "asperity" model developed by *Dreger and Helmberger* [1991]. In this model, 70% of the total moment comes from uniform slip on on a fault patch 3.5 km square, at the bottom of the fault plane we have imaged, with the rest distributed over the whole plane. Third, we include the large aftershock ($M_L = 4.7$) 3 hours after the 1990 mainshock, assuming uniform slip and a fault plane given either by model 2 or model 3. Because the stress change is dominated by the moment release from the mainshock, the pattern of ΔCFS depends very little on this last choice; we show results for the plane found in model 3.

Figure 11 shows horizontal sections of ΔCFS, computed for optimally oriented planes within an ambient stress field with maximum compression of -100 bars north-south and maximum tension of 100 bars east-west. This assumed background stress field is in agreement with stress directions found by *Hauksson and Jones* [1990] and is consistent with other stress determinations in this part of the Los Angeles basin. The magnitude of the ambient stress field has little influence on the results shown in Figure 11, provided the stress is larger than a few bars (i.e., much larger than the coseismic stress changes). The background stress field determines the optimal failure plane for each possible aftershock location; the coseismic stress changes then either increase or decrease the Coulomb failure stress across these planes. According to the static stress triggering model, positive ΔCFS values should increase the probability of aftershocks, whereas negative ΔCFS values should reduce the aftershock probability. For comparison, Figure 11 shows the seismicity within ranges of ±1 km from the depths of the sections. The most notable feature is that while ΔCFS is approximately symmetric under a 180° rotation, the seismicity is not: as Figure 10 also shows, most of the off-fault aftershocks

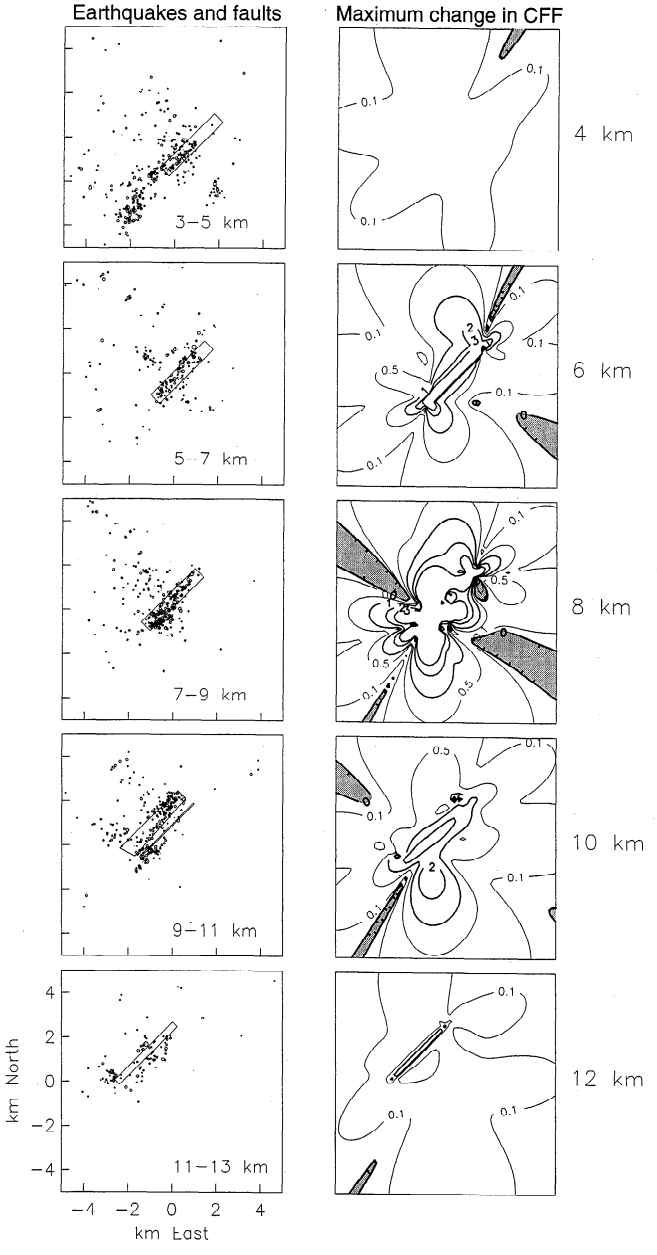

Figure 11. (right) The change in Coulomb failure stress, ΔCFS, at even depths from 4 to 12 km resulting from model 3 parameters listed in Table 3. Background stresses are T_{NS} = -100 bars, T_{EW} = 100 bars, and zero vertical stress. (left) The 2-km depth slices of our relocated seismicity centered at depths corresponding to the stress change calculations. The cross section of the fault plane at each depth slice is also shown. There is no clear correlation between the aftershock locations and regions with positive ΔCFS values, as might have been expected if static stress changes were triggering the aftershocks.

are northwest of the main rupture surface. It thus appears for the Upland sequence that ΔCFS is not a good predictor of aftershock locations. Because the moment release of the 1990 mainshock is much larger than any of the other earthquakes in the Upland sequence, this conclusion is robust with respect to uncertainties in the orientations of the smaller events (such as those shown in Figure 10).

10. Conclusions

We attempt to map the fault geometry of the poorly defined San Jose fault located in the eastern San Gabriel Mountains in southern California from precise relocations of events occurring in the vicinity of the 1988 ($M = 4.7$) and the 1990 ($M = 5.5$) Upland earthquakes. We apply an L1 norm grid search algorithm with station terms to account for the three-dimensional velocity structure outside the region. Existing pick information from the SCSN analysts is supplemented using precise P and S differential times obtained through waveform cross correlation of similar event pairs. Our final results indicate that locations of the +1-month aftershocks of the 1988 Upland ($M = 4.7$) delineate a fault with a dip angle of ~45° between 7 and 9 km depth, consistent with previously determined focal mechanisms for this event. This lineation of events seems to offset a steeper fault of ~75° dip, as shown by relocations of aftershocks of the 1990 Upland earthquake that corresponds to the inferred location of the San Jose fault. We discuss three different fault geometries that are roughly consistent with our relocations and focal mechanism solutions. We use these together with slip models to compute the stress change from the larger events in the sequence, and we compute the change in Coulomb failure stress on faults best oriented for failure. The pattern of this change is nearly symmetric about the main rupture plane, unlike the off-fault aftershocks, which mostly occur northwest of that plane. This suggests that simple models of static stress triggering by mainshocks are not useful in explaining the distribution of Upland aftershocks. The asymmetry in the aftershock distribution is more likely a result of differences in the rock properties bounding the fault. Although the static stress triggering model has proven significant in some cases [e.g., *King et al.*, 1994; *Stein et al.*, 1994; *Hodgkinson et al.*, 1996], our results show that it is not always a good predictor of aftershock locations. A similiar conclusion was recently obtained by *Hardebeck et al.* [1998] for the first month of aftershocks of the 1994 Northridge earthquake. The evidence suggesting that the San Jose fault may separate different lithologies at depth is very limited [*Woodford et al.*, 1944]. Because it has been mapped on the basis of a water barrier [*California Department of Water Resources*, 1970], it is possible that the fluid content may change across the San Jose fault, and this difference may be responsible for the asymmetry in the aftershock distribution of the Upland events.

Acknowledgments. We thank the personnel of the USGS/Caltech Southern California Seismic Network who pick and archive the seismograms and the Southern California Earthquake Center for distributing the data; we es-

pecially thank Katherine Hafner, who facilitated access to the database. We also thank Gary Pavlis, Joan Gomberg, and Michael Hamburger for critical reviews that improved the final manuscript. This work was supported by the Southern California Earthquake Center. SCEC is funded by NSF Cooperative Agreement EAR-8920136 and USGS Cooperative Agreements 14-08-001-A0899 and 1434-HQ-97AG01718. The SCEC contribution number for this paper is 490. This research was also funded by NEHRP/USGS grants 1434-94-G-2454 and 1434-HQ-97-GR-03162.

References

Anderson, K.R., Robust earthquake location using M-estimates, *Phys. Earth Planet. Inter., 30*, 119-130, 1982.

Aster, R.C., and J. Scott, Comprehensive characterization of waveform similarity in microearthquake data sets, *Bull. Seismol. Soc. Am., 83*, 1307–1314, 1993.

Billings, S.D., M.S. Sambridge, and B.L.N. Kennett, Errors in hypocenter location: Picking, model, and magnitude dependence, *Bull. Seismol. Soc. Am., 84*, 1978–1990, 1994.

Braun, J., and M. Sambridge, A numerical method for solving partial differential equations on highly irregular evolving grids, *Nature, 376*, 655–660, 1995.

California Department of Water Resources, Meeting water demands in the Chino-riverside area, Appendix A—Water supply, *Bull. Calif. Dep. Water Resour., 104-3*, 1–108, 1970.

Constable, C.G., R.L. Parker, and P.B. Stark, Geomagnetic field models incorporating frozen flux constraints, *Geophys. J. Int., 113*, 419–433, 1993.

Cramer, C.H., and J.M. Harrington, Seismicity and tectonics of the Cucamonga Fault and the eastern San Gabriel Mountains, San Bernardino County, in *Recent Reverse Faulting in the Transverse Ranges, CA*, edited by D.M. Martin and R.F. Yerkes, *U.S. Geol. Surv. Prof. Pap., 1339*, 7–26, 1987.

Deichmann, N., and M. Garcia-Fernandez, Rupture geometry from high-precision relative hypocentre locations of microearthquake ruptures, *Geophys. J. Int., 110*, 501–517, 1992.

Dodge, D.A., G.C. Beroza, and W.L. Ellsworth, Detailed observations of California foreshock sequences: Implications for the earthquake initiation process, *J. Geophys. Res., 101*, 22,371–22,392, 1996.

Dreger, D.S., and D.V. Helmberger, Broadband modeling of local earthquakes, *Bull. Seismol. Soc. Am., 80*, 1162–1179, 1990.

Dreger, D.S., and D.V. Helmberger, Complex faulting deduced from broadband modeling of the 28 February 1990 Upland earthquake (M_L=5.2), *Bull. Seismol. Soc. Am., 81*, 1129–1144, 1991.

Erickson, L.E., A three-dimensional dislocation program with applications to faulting in the Earth, M.S. thesis, 167 pp., 1986. Dept. of Appl. Earth Sci., Stanford Univ.

Feigl, K. L., et al., Space geodetic measurement of crustal deformation in central and southern California, 1984-1992, *J. Geophys. Res., 98*, 21,677–21,712, 1993.

Fremont, M.-J., and S.D. Malone, High precision relative locations of earthquakes at Mount St. Helens, Washington, *J. Geophys. Res., 92*, 10,223–10,236, 1987.

Frohlich, C., An efficient method for joint hypocenter determination for large groups of earthquakes, *Comput. Geosci., 5*, 387–389, 1979.

Gillard, D., A.M. Rubin, and P. Okubo, Highly concentrated seismicity caused by deformation of Kilauea's deep magma system, *Nature, 384*, 343–346, 1996.

Gomberg, J.S., K.M. Shedlock, and S.W. Roecker, The effect of S-wave arrival times on the accuracy of hypocenter location, *Bull. Seismol. Soc. Am., 80*, 1605–1628, 1990.

Got, J.-L., J. Fréchet, and F.W. Klein, Deep fault plane geometry inferred from multiplet relative relocation beneath the south flank of Kilauea, *J. Geophys. Res., 99*, 15,375–15,386, 1994.

Haase, J.S., P.M. Shearer, and R.C. Aster, Constraints of temporal variations in velocity near Anza, California, from analysis of similar event pairs, *Bull. Seismol. Soc. Am., 85*, 194–206, 1995.

Hadley, D.M., and H. Kanamori, Seismic structure of the Transverse Ranges, California, *Geol. Soc. Am. Bull., 88*, 1461–1478, 1977.

Hardebeck, J.L., J.J. Nazareth, and E. Hauksson, The static stress change triggering model: Constraints from two southern California aftershock sequences, *J. Geophys. Res., 103*, 24,427–24,437, 1998.

Harris, R.A., Introduction to special section: stress triggers, stress shadows, and implications for seismic hazard, *J. Geophys. Res., 103*, 24,347–24,358, 1998.

Harris, R.A., and R.W. Simpson, Changes in static stress on southern California faults after the 1992 Landers earthquake, *Nature, 360*, 251–254, 1992.

Hauksson, E., Earthquakes, faulting, and stress in the Los Angeles Basin, *J. Geophys. Res., 95*, 15,365–15,394, 1990.

Hauksson, E., and L.M. Jones, The 1987 Whittier Narrows earthquake sequence in Los Angeles, southern California: Seismological and tectonic analysis, *J. Geophys. Res., 94*, 9569–9589, 1989.

Hauksson, E., and L.M. Jones, The 1988 and 1990 Upland earthquakes: Left-lateral faulting adjacent to the Central Transverse Ranges, *J. Geophys. Res., 96*, 8143–8165, 1991.

Hauksson, E., L.M. Jones, and K. Hutton, The 1994 Northridge earthquake sequence in California: Seismological and tectonic aspects, *J. Geophys. Res., 100*, 12,335–12,355, 1995.

Hildebrand, J.A., and R.L. Parker, Paleomagnetism of Cretaceous seamounts revisited, *J. Geophys. Res., 92*, 12,695–12,712, 1987.

Hodgkinson, K. M., R.S. Stein, and G.C.P. King, The 1954 Rainbow Mountain-Fairview Peak-Dixie Valley earthquakes: A triggered normal faulting sequence, *J. Geophys. Res., 101*, 25,459–25,471, 1996.

Humphreys, E., Tectonics of the greater Los Angeles region: Implications for the lower crust and upper mantle, *EOS Trans. AGU, 76 (46), Fall Meet. Suppl.*, F347, 1995.

Ito, A., High resolution relative hypocenters of similar earthquakes by cross-spectral analysis method, *J. Phys. Earth, 33*, 279–294, 1985.

Jones, L.M., K.E. Sieh, E. Hauksson, and L.K. Hutton, The 3 December 1988 Pasadena, California earthquake: Evidence for strike-slip motion on the Raymond fault, *Bull. Seismol. Soc. Am., 80*, 474–482, 1990.

Kanamori, H., and D. L. Anderson, Theoretical basis of some empirical relations in seismology, *Bull. Seismol. Soc. Am., 65*, 1073–1095, 1975.

Kennett, B.L.N., Locating oceanic earthquakes—The influence of regional models and location criteria, *Geophys. J. Int., 108*, 848–854, 1992.

Kijko, A., Seismological outliers: L_1 or adaptive L_p norm application, *Bull. Seismol. Soc. Am., 84*, 473–477, 1994.

King, G.C.P., R.S. Stein, and J. Lin, Static stress change and the triggering of earthquakes, *Bull. Seismol. Soc. Am., 84*, 935–953, 1994.

Mezcua, J., and J. Rueda, Earthquake relative location based on waveform similarity, *Tectonophysics, 233*, 253–263, 1994.

Mori, J., and S. Hartzell, Source inversion of the 1988 Upland, California, earthquake: Determination of a fault plane for a small event, *Bull. Seismol. Soc. Am.*, *80*, 507–518, 1990.

Morton, D. M., and J.C. Matti, The Cucamonga fault zone: Geological setting and Quaternary history, in *Recent Reverse Faulting in the Transverse Ranges, CA*, edited by D.M. Martin and R.F. Yerkes, *U.S. Geol. Surv. Prof. Paper, 1339*, 179–203, 1987.

Nadeau, R.M., W. Foxall, and T.V. McEvilly, Clustering and periodic recurrence of microearthquakes on the San Andreas Fault at Parkfield, California, *Science*, *267*, 503–507, 1995.

Parker, R.L., L. Shure, and J.A. Hildebrand, The application of inverse theory to seamount magnetism, *Rev. Geophys.*, *25*, 17–40, 1987.

Pavlis, G.L., Appraising earthquake hypocenter location errors: A complete practical approach for single event locations, *Bull. Seismol. Soc. Am.*, *76*, 1699–1717, 1986.

Pavlis, G.L., Appraising relative earthquake location errors, *Bull. Seismol. Soc. Am.*, *82*, 836–859, 1992.

Pechmann, J., Tectonic implications of small earthquakes in the central Transverse ranges, in *Recent Reverse Faulting in the Transverse Ranges, CA*, edited by D.M. Martin and R.F. Yerkes, *U.S. Geol. Surv. Prof. Paper, 1339*, 97–112, 1987.

Pechmann, J.C., and H. Kanamori, Waveform and spectra of preshocks and aftershocks of the 1979 Imperial Valley, California, earthquake: A test of the asperity model, *J. Geophys. Res.*, *87*, 10,579–10,597, 1982.

Pechmann, J.C., and B.S. Thorbjarnrdottir, Waveform analysis of two preshock–main shock–aftershock sequences in Utah, *Bull. Seismol. Soc. Am.*, *80*, 519–551, 1990.

Poupinet, G., W.L. Ellsworth, and J. Frechet, Monitoring velocity variations in the crust using earthquake doublets: An application to the Calaveras Fault, California, *J. Geophys. Res.*, *89*, 5719–5731, 1984.

Reasenberg, P.A., and R.W. Simpson, Response of regional seismicity to the static stress change produced by the Loma Prieta earthquake, *Science*, *255*, 1687–1690, 1992.

Roecker, S.W., and W.L. Ellsworth, VELEST, FORTRAN Program, U.S. Geol. Surv., Menlo Park, Calif., 1978.

Rubin, C.M., S.C. Lindvall, and T.K. Rockwell, Evidence for large earthquakes in metropolitan Los Angeles, *Science*, *281*, 398–402, 1998.

Sambridge, M.S., and B.L.N. Kennett, A novel method of hypocentre location, *Geophys. J. R. Astron. Soc.*, *87*, 679–697, 1986.

Sambridge, M.J. Braun, and H. McQueen, Geophysical parameterization and interpolation of irregular data using natural neighbors, *Geophys. J. Int.*, *122*, 837–857, 1995.

Shaw, J.H. and P.M. Shearer, An elusive blind-thrust fault beneath metropolitan Los Angeles, *Science*, *283*, 1516–1518, 1999.

Shearer, P.M., Improving local earthquake locations using the L1 norm and waveform cross correlation: Application to the Whittier Narrows, California, aftershock sequence, *J. Geophys. Res.*, *102*, 8269–8283, 1997.

Shearer, P.M., Evidence from a cluster of small earthquakes for a fault at 18 km depth beneath Oak Ridge, southern California, *Bull. Seismol. Soc. Am.*, *88*, 1327–1336, 1998.

Stein, R.S., G.C.P. King and J. Lin, Change in failure stress on the southern San Andreas fault system caused by the 1992 magnitude = 7.4 Landers earthquake, *Science*, *258*, 1328–1332, 1992.

Stein, R.S., G.C.P. King, and J. Lin, Stress triggering of the 1994 M=6.7 Northridge, California, earthquake by its predecessors, *Science*, *265*, 1432–1435, 1994.

Walls, C., T. Rockwell, K. Muellers, Y. Bock, S. Williams, J. Pfanner, J. Dolan, and P. Fang, Escape tectonics in the Los Angeles metropolitan region and implications for seismic risk, *Nature*, *394*, 356–360, 1998.

Woodford, A.O., J.S. Sheton, and T.G. Moran, Geology and oil possibilities of Puente and San Jose Hills, CA, *U.S. Geol. Surv. Oil Gas Invest., Prelim. Map*, 23, 1944.

Xie, J., Z. Liu, R.B. Herrmann, and E. Cranswick, Source processes of three aftershocks of the 1983 Goodnow, New York, earthquake: High resolution images of small symmetric ruptures, *Bull. Seismol. Soc. Am.*, *81*, 818–843, 1991.

D.C. Agnew, L. Astiz, and P.M. Shearer, IGPP 0225, Scripps Institution of Oceanography, University of California, San Diego, La Jolla, CA, 92093-0225 (pshearer@ucsd.edu).

(Received October 16, 1998; revised August 25, 1999; accepted September 16, 1999.)